Interaction of Genetic Variants Activates Latent Metabolic Pathways in Yeast

Srijith Sasikumar[1,2,3], Shannara Taylor Parkins[4], Suresh Sudarsan[4], Himanshu Sinha[1,2,3,*]

[1]Systems Genetics Lab, Department of Biotechnology, Bhupat and Jyoti Mehta School of Biosciences, [2]Centre for Integrative Biology and Systems Medicine (IBSE), [3]Wadhwani School of Data Science and Artificial Intelligence (WSAI), Indian Institute of Technology Madras, Chennai, Tamil Nadu, India

[4]The Novo Nordisk Foundation Center for Biosustainability, Technical University of Denmark, DK-2800 Kgs. Lyngby, Denmark

[*] Corresponding author: Himanshu Sinha sinha@iitm.ac.in

ABSTRACT

Genetic interactions are prevalent across species, from yeast to humans, and play a crucial role in shaping complex traits. However, the molecular mechanisms underlying these interactions remain largely unexplored. Here, we answer the question of whether interactions between genetic variants can activate novel unique pathways and if such pathways can be targeted to modulate phenotypic outcomes. The model organism *Saccharomyces cerevisiae* was used to investigate the interaction between two key SNPs, $MKT1^{89G}$ and $TAO3^{4477C}$, during sporulation, a complex dynamic metabolic process. By integrating temporal gene expression and proteomics data, we show that these SNPs, in combination, activate amino acid metabolism, particularly the arginine biosynthesis pathway, while downregulating ribosome biogenesis, an energy-intensive process in response to nutrient starvation. This metabolic trade-off reveals a key mechanism by which SNP interactions modulate cellular responses to environmental stress, thereby enhancing sporulation. Further, the essential role of the arginine biosynthetic pathway in maintaining mitochondrial activity when these SNPs interact has been validated experimentally with deletion mutants. Our findings illustrate a broader impact beyond yeast, especially on complex human metabolic diseases like cancer, where specific SNP combinations hyperactivate ribosomal pathways while suppressing metabolic pathways that usually control cell growth, leading to uncontrolled proliferation.

Keywords: Sporulation, single nucleotide polymorphism, amino acid metabolism, ribosome pathways, proteomics, transcriptomics, yeast

INTRODUCTION

Complex traits arise from intricate interactions between causal genetic loci, the broader genetic background, and environmental influences[1,2]. These loci can influence traits through additive genetic effects or non-additive interactions, such as dominance and epistasis. Several studies have focused on mapping genetic interactions in model organisms like yeast[3–8] and human diseases[9–13]. A global genetic interaction network for yeast employing reverse genetic screens on essential and non-essential genes revealed numerous genetic interactions, with many interacting genes belonging to the same functional pathways, forming highly organised and structured genetic networks[6]. Similarly, CRISPR knockout screens have identified genes essential for cell viability in cancer and pluripotent stem cells in human cell lines[14]. While most studies have focused on gene deletions or knockouts to identify genetic networks, a few have used biparental yeast populations to find genetic networks among gene variants[7,15]. These studies identified variant-specific gene networks that had environment-sensitive genetic interactions, and incorporating such genetic interactions into predictive models of phenotypic variation significantly improved their accuracy.

While the above-mentioned studies highlight the prevalence of genetic interactions in shaping complex traits, a crucial gap remains in understanding how these interactions function at the molecular level. Specifically, how do genetic variants interact to modulate molecular pathways and contribute to phenotypic variation? Addressing this question is essential for identifying novel functional targets that can be leveraged to modulate complex traits, particularly in diseases influenced by multiple interacting variants[16,17]. In this study, we sought to test the hypothesis: do interacting single nucleotide polymorphisms (SNPs) function independently through their respective functional networks, or do they activate novel molecular pathways when combined (Figure 1A)?

There are several challenges in studying genetic interactions between SNPs, particularly in complex traits. First, genetic background can confound the effect of SNP interactions[5,18,19]. Second, while gene expression has been widely studied, its correlation with protein levels is often limited[20,21]. Third, biological processes and the intermediate phenotypes underpinning these processes are dynamic[22].

To overcome these challenges, we employed *Saccharomyces cerevisiae*, a yeast model system, where one can use isogenic allele replacement yeast strains to study various complex traits and

identify the phenotypic and molecular effects of genetic variants at the single-nucleotide level[3,23,24]. Gene expression changes alone may not fully explain phenotypic outcomes, as protein expression and post-translational modifications frequently play critical roles. A systems genetics approach of integrating multi-omics data, such as transcriptomics, proteomics, and metabolomics, offers a framework for overcoming the challenge of understanding the complex interplay among these intermediate phenotypes and their impact on biological processes[25,26]. In recent studies, the integration of multi-omics information has guided targeted therapies in discovering biomarkers for cancers and other complex diseases[27–33]. Furthermore, studies in model organisms[34–40] and humans[41] have demonstrated that gene and protein expression variations are highly context-specific, varying by developmental stage. Despite significant advances, most studies investigating the molecular basis of genetic interactions in yeast have focused on gene expression at a single time point[42,43]. Therefore, understanding the temporal phase during which causal genetic variants exert their molecular effects is critical for understanding genotype-phenotype relationships[36,39,40].

We designed a study to systematically investigate the genetic interaction between two key quantitative trait loci (QTLs) in yeast sporulation, a developmental process. Using isogenic yeast strains carrying distinct SNPs, individually and in combination, we integrated temporal transcriptomic and proteomic data to capture gene expression and protein level changes at multiple time points during sporulation (Figure 1B). This allowed us to compare the effects of individual SNPs with their combined effects, revealing how SNP interactions modulate molecular pathways over time. Our results showed that the combination of SNPs activated a novel metabolic pathway, different from those activated by each SNP independently. Our findings have broader implications for understanding polygenic traits and diseases, where multiple SNPs contribute additively to phenotypic variation. We provide critical insights into the regulatory mechanisms underlying complex traits by dissecting how causal SNPs interact at the molecular level. This knowledge can inform the development of therapeutic strategies for diseases driven by polygenic interactions, offering new avenues for targeted interventions.

RESULTS

Role of *MKT1*^{89G} and *TAO3*^{4477C} *SNPs* in sporulation efficiency variation

Sporulation is a developmentally regulated metabolic process in yeast. In response to nutrient limitations, such as nitrogen starvation and the availability of a non-fermentable carbon source

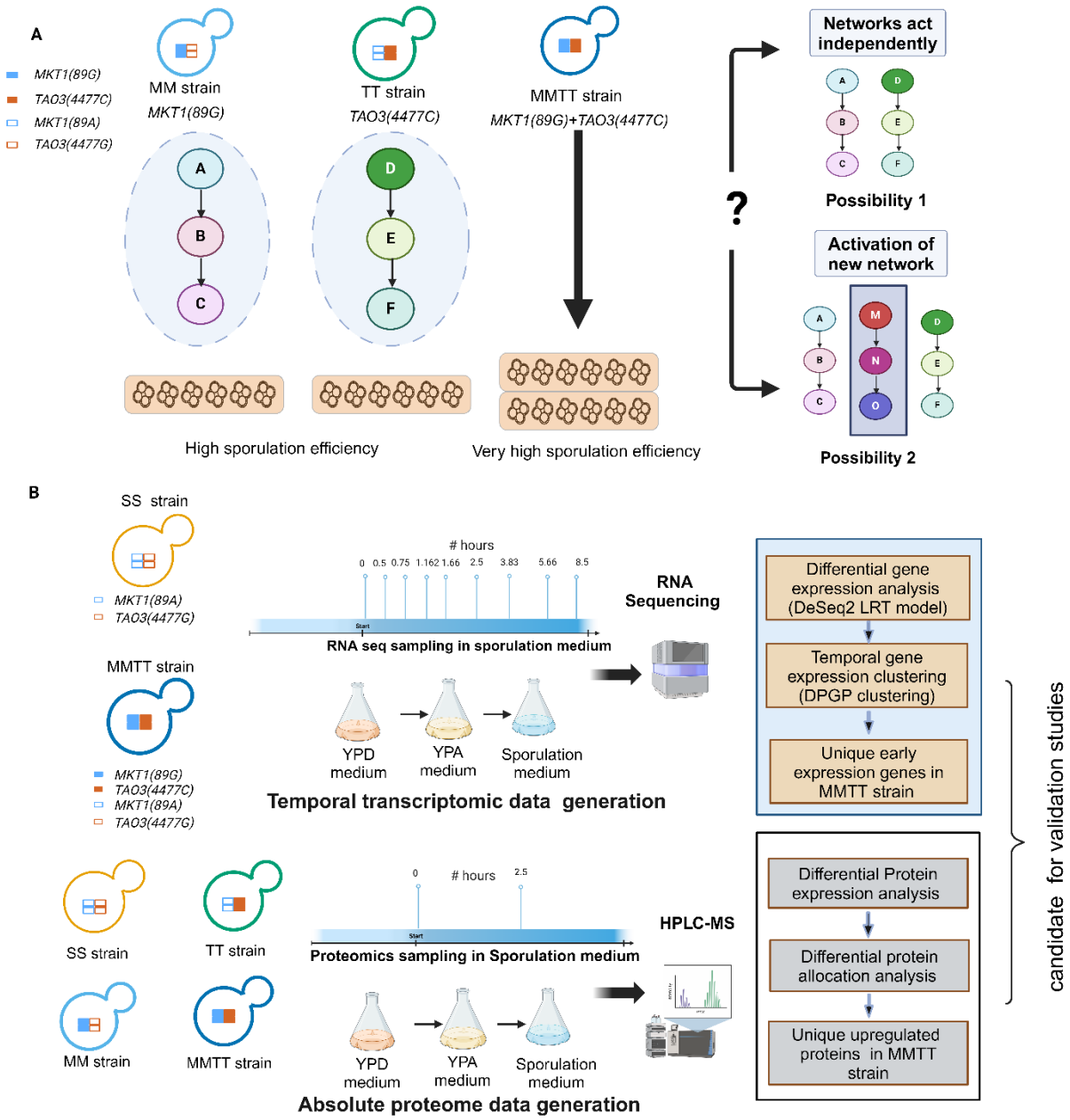

Figure 1: Overview of the model under study

(A) Illustration of the proposed molecular mechanism involving *MKT1*^{89G} and *TAO3*^{4477C}. This panel highlights the potential interaction between the gene and protein expression networks of *MKT1*^{89G} and *TAO3*^{4477C}, contributing to the observed additive effect on higher sporulation efficiency. (B) Schematic representation of the study design for temporal transcriptomics and proteomics analysis of yeast strains in sporulation medium. This panel outlines the experimental approach to identify the molecular mechanisms underlying the phenotypic additivity observed in the yeast strains.

like acetate, diploid yeast cells undergo meiosis, ultimately producing four haploid spores[44]. Sporulation efficiency, defined as the rate of spore formation, is a quantitative trait in yeast and is well-studied[34,35,45–47]. A previous study by Deutschbauer and Davis[24] identified *MKT1*^{89G} and *TAO3*^{4477C} SNPs from the high sporulating strain, SK1, as causal for increasing sporulation efficiency of the low sporulating strain, S288c. To study the phenotypic effects of these two SNPs, we used a panel of isogenic strains in the S288c background generated by swapping specific S288c nucleotides with their SK1 allele counterparts, resulting in four diploid strains: wildtype S288c, hereafter referred to as SS strain, MM strain with the *MKT1*^{89G} SNP, TT strain with the *TAO3*^{4477C} SNP, and MMTT strain harbouring both *MKT1*^{89G} and *TAO3*^{4477C} SNPs in combination (Figure 2A). Under the conditions described, we first measured the sporulation efficiencies of these allele replacement strains to assess the effects of SNPs on sporulation efficiency variation. The MM, TT, MMTT, and MmTt allele replacement strains and the wildtype SK1 strain exhibited increased sporulation efficiency after 48 hours in a sporulation medium compared to the S288c strain (Figure 2B), consistent with previous reports[24,39,40]. We confirm that the sporulation efficiency of the MMTT and MmTt strains was additive, representing the sum of individual sporulation efficiencies of the MM and TT strains. Furthermore, we observed that the *MKT1*^{89G} and *TAO3*^{4477C} alleles dominate over the S288c alleles *MKT1*^{89A} and *TAO3*^{4477G} (Figure 2B).

The increased sporulation efficiency of the allele replacement strains could be due to better nutrient uptake properties of the SNPs. Sporulation in yeast is induced when the yeast strains are grown in a medium where the sole carbon source is acetate. To investigate if the observed phenotypic variation resulted from differences in acetate uptake, we measured the extracellular acetate levels in the sporulation medium at the initial phase (30m), early phase (2h30m), and at 24h. We observed that the acetate levels in the sporulation medium remained consistent for all four strains at the measured time points. Additionally, we found a decrease in acetate levels across all four strains at 24h due to its utilisation (Figure 2C). This observation suggested that the additive phenotypic effect was not due to the acetate utilisation but to an underlying gene and protein expression change, including the specific SNPs and their interactions.

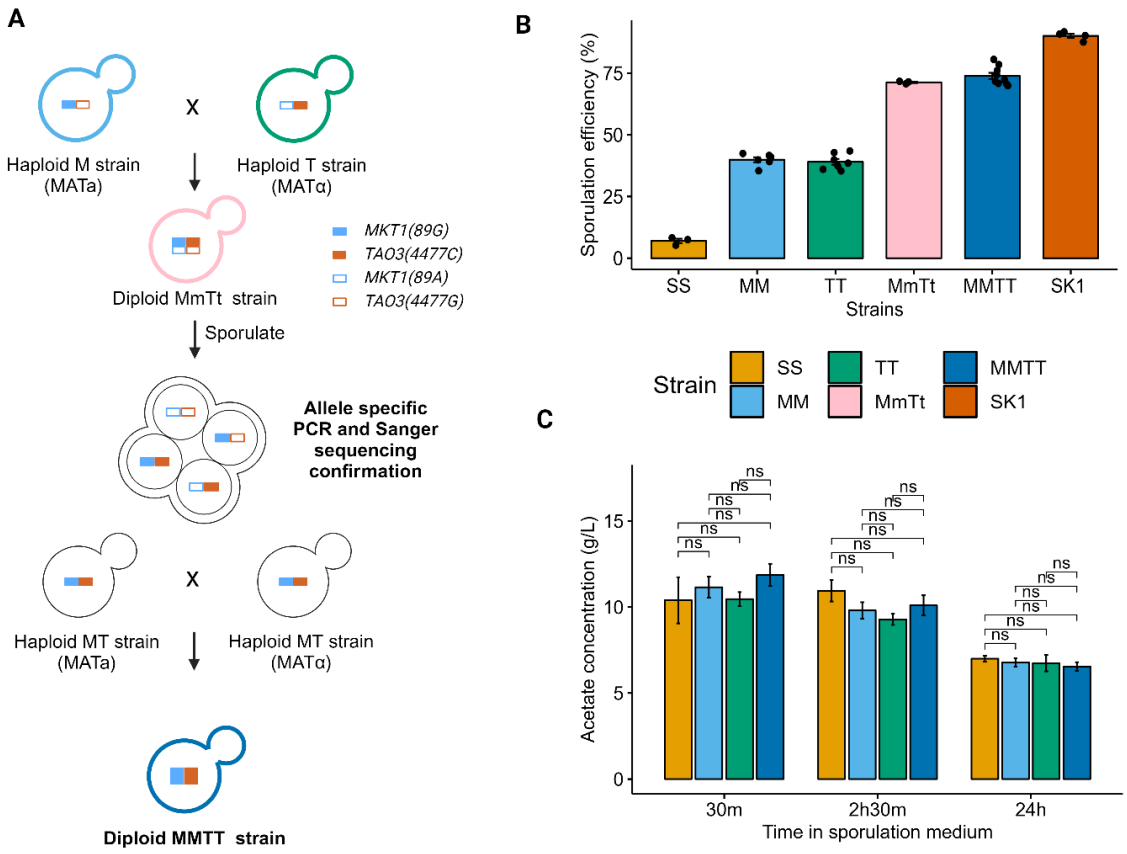

Figure 2: Additive effect of *MKT1*^{89G} and *TAO3*^{4477C} *in* sporulation efficiency variation

(A) Schematic representation of the steps involved in generating the MT strain, highlighting the introduction of the *MKT1*^{89G} and *TAO3*^{4477C} alleles. (B) Sporulation efficiency of the S, M, T, MT, MmTt (heterozygous), and SK1 strains was measured after 48h in the sporulation medium. The bar graph represents the percentage of sporulating cells (dyads, triads and tetrads), demonstrating the additive effect of the *MKT1* and *TAO3* alleles. (C) Extracellular acetate levels in the sporulation medium of the S, M, T, and MT strains were measured using HPLC at three time points: 30min, 2h30min, and 24h. P-values were calculated using an unpaired t-test in the rstatix R package (v.0.7.2). Significance levels are indicated as follows: **** $p < 1e-4$, *** $p < 1e-3$, ** $p < 1e-2$, * $p < 5e-2$, and ns (not significant) for $p > 5e-2$. The mean ± s.d. of three biological replicates is shown.

Temporal reshuffling of amino acid metabolism and ribosomal pathways in the presence of *MKT1^{89G}* and *TAO3^{4477C}* combination

In previous studies from our lab, we investigated the functional and molecular effects of the *MKT1^{89G}* and *TAO3^{4477C}* SNPs using global temporal microarray analyses, with samples collected throughout sporulation up to 8h30m, with denser sampling during the early stages. These studies revealed that *MKT1* and *TAO3* play critical roles early in sporulation. The *MKT1^{89G}* allele enhanced sporulation efficiency by activating genes such as *RTG1/3*, which is involved in mitochondrial retrograde signalling, and *DAL82*, associated with nitrogen starvation[39]. In contrast, the *TAO3^{4477C}* allele improved sporulation efficiency through the activation of genes like *ERT1*, linked to the tricarboxylic acid (TCA) cycle, and *PIP2*, involved in gluconeogenesis, compared to when these SNPs were absent[40].

To characterise the effect of *MKT1^{89G}* and *TAO3^{4477C}* SNPs in the combination on the global gene expression variation, we performed RNAseq for SS strain and MMTT strain throughout sporulation with denser sampling during the early phase at 0h, 30m, 45m, 1h10m, 1h40m, 2h30m, 3h50m, 5h40m till 8h30m (Figure 3A). These time points were identical to the expression analysis study done for single SNP strains, MM and TT, which allowed us to make comparisons of differentially expressed genes between individual SNPs and their combinations to identify causal mechanisms activated in response to genetic interactions.

Hierarchal clustering and Principal component analysis (PCA) of the gene expression data revealed a clear distinction between the SS and MMTT strains (Figure S1A-B). The analysis of differentially expressed genes at each time point against the initial time point between SS and MMTT strains revealed substantial differences in gene expression patterns between the two strains. The differentially expressed genes at each time point for SS and MMTT strains are provided in Table S3. A notable increase in DEGs was observed in the MMTT strain, particularly during the early phase (2h30m), with 132 genes upregulated and 32 downregulated. This trend continued in the later phase (8h30m), where 265 genes were upregulated, and 61 were downregulated (Figure 3B). GO enrichment analysis on the upregulated and downregulated genes found that in the case of the S strain, there was a consistent upregulation of pathways like protein folding, response to heat (stress response), and biosynthesis of amino acids across all time points. In contrast, the MMTT strain exhibited distinct pathway activations

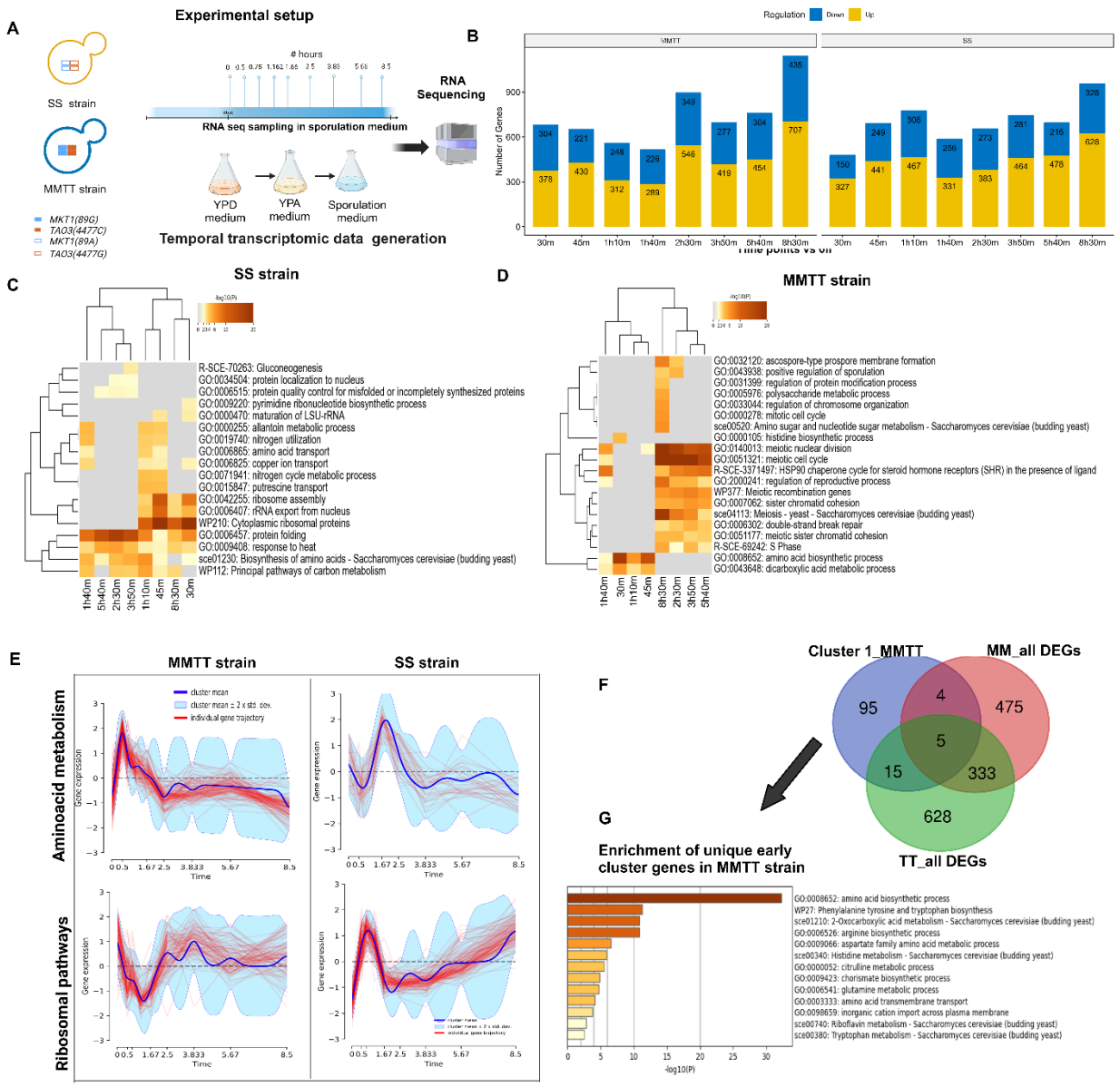

Figure 3: Temporal reshuffling of amino acid metabolism and ribosomal pathways in the presence of *MKT1*^{89G} and *TAO3*^{4477C} SNPs.

(A) Schematic representation of the design of the time series RNA sequencing experiment. This panel illustrates the overall experimental setup, including collecting RNA samples from S288c and MMTT strains at nine time points during sporulation. (B) The bar graph represents the number of differentially expressed genes at each time point compared to the 0th hour for both S288c and MMTT strains. The data is represented with a significance threshold of adjusted p-value < 0.05 and log fold change (LFC) > |2|. (C-D) Gene Ontology (GO) enrichment analysis for upregulated genes in S288c and MMTT strains at each time point. The heatmaps represent the p-values of enriched GO terms, with clustering performed on rows (GO terms) and columns (time points). (E)Temporal expression trajectories of genes

involved in Amino-acid metabolism and ribosomal related pathways in SS and MMTT strain along with cluster mean and ±2 standard deviations (F) Venn diagram analysis between early cluster genes In MMTT (Cluster 1) and DEGs from MM and TT strains (G) Enrichment analysis of unique early cluster genes In MMTT strains.

between early time points (30m, 45m, 1h10m, 1h40m) and middle to late time points (2h30m, 3h50m, 5h40m, 8h30m). Specifically, significant upregulation was observed in genes associated with the amino acid biosynthetic process, dicarboxylic acid metabolic process, and histidine biosynthetic process as early as 30 minutes into sporulation (Figure 3C). These pathways remained upregulated during the early phase but not in the middle and late phases. Additionally, the enrichment of pathways related to meiotic nuclear division and the meiotic cell cycle began at 1h40m in the MMTT strain, which was not observed in the S strain. Furthermore, genes involved in polysaccharide metabolic processes and ascospore-type pro-spore membrane formation were uniquely upregulated at 8h30m in the MMTT strain, highlighting the onset of spore wall formation (Figure 3C).

In addition, we identified a set of genes that were differentially expressed as a function of the *MKT1*^{89G} and *TAO3*^{4477C} genotypes in combination over time. The DESeq2[48] LRT method was applied with a full model that included genotype + time + genotype: time and a reduced model that included only genotype + time. This analysis identified 1,080 differentially expressed genes with an adjusted p-value of 0.001 (Table S4). These genes were primarily enriched in pathways related to the meiotic cell cycle, cytoplasmic ribosomal proteins, amino acid metabolic processes, and ribosome biogenesis (Figure S2A).

To understand the temporal trajectories that vary between the SS and MMTT strains, we performed clustering using the Dirichlet Gaussian process mixture model (DPGP)[49]. Based on recent studies that have established the effectiveness of the Dirichlet process Gaussian process mixture model (DPGP) in identifying co-regulated genes within transcriptomic datasets, we applied DPGP clustering independently to the expression values of these 1,080 differentially expressed transcripts for both the SS and MMTT strains. In brief, DPGP clusters the data using the Dirichlet process while modelling the temporal dependencies with Gaussian processes. This analysis resulted in 17 clusters for the MMTT and 18 for the SS strain. The genes in each cluster for the two strains are detailed in Table S5. The clusters were then analysed for enrichment to specific biological processes using Metascape (Figure S2B-C). Given the

importance of early response genes in determining sporulation efficiency variation, the GO enrichment for the early cluster genes was specifically examined. In the SS strain, clusters 5 and 9 (Figure S2B, Figure S3), which showed early expression trajectories, were enriched for ribosome-related pathways, with 49 and 121 genes, respectively (Figure 3E). In the MMTT strain, cluster 5, enriched for ribosome-related pathways, exhibited the downregulation of genes during the early phase (Figure 3E).

We also observed that cluster 1 in the MMTT strain, enriched for amino acid metabolism genes, showed an early expression trend (Figure 3E). In comparison, these pathways in the SS strain displayed an initial downregulation followed by delayed upregulation (Figure 3E). This pattern suggested a trade-off in the MMTT strain between the amino acid biosynthetic process and ribosomal pathways. Since ribosome biogenesis was an energy-intensive process, the MMTT strain appeared to downregulate ribosome-related genes and upregulate amino acid metabolism in response to sporulation conditions, possibly to enhance sporulation efficiency, a strategy not observed in the SS strain.

We then examined the active genes in the later stages of sporulation. As expected, clusters 2 and 3 in the MMTT strain, which showed increased and synchronised gene expression in the later phase, were enriched for meiosis-related pathways, cell cycle regulation, and prospore membrane formation (Figure S2B, S4B). This differed from SS, where these genes did not display any specific temporal gene expression pattern (Figure S4B). This finding demonstrated how the combination of $MKT1^{89G}$ and $TAO3^{4477C}$ reshuffled the trajectories of amino acid metabolism and ribosomal pathways to facilitate efficient sporulation in the MMTT strain.

Finally, we aimed to identify genes that exhibit early expression trends in the MMTT strain but do not show differential expression in the MM and TT strains. These genes are interesting because their expression likely results from genetic interactions of $MKT1^{89G}$ and $TAO3^{4477C}$ specific to the MMTT strain and could be causal for the sporulation efficiency variation. Comparison of the differentially expressed genes identified for the MM and TT strains, as reported in the original publications, with the 119 genes in cluster 1 of the MMTT strain revealed 95 genes unique to the MMTT strain, which were enriched in pathways related to amino acid biosynthesis, including phenylalanine, tyrosine, and tryptophan biosynthesis, 2-oxocarboxylic acid metabolism, and arginine biosynthesis (Figure 3F-G). These findings underscore a distinct transcriptional response in the MMTT strain during sporulation to an

immediate response to nitrogen starvation, driven by the genetic interactions between the *MKT1*^{89G} and *TAO3*^{4477C} SNPs, which enhanced sporulation efficiency.

A limited but function-specific correlation between transcript and protein levels

Transcript abundance and protein level correlations are poorly correlated[20,21]. In this and previous studies[34,39,40], specific functional categories of gene sets are differentially and temporally regulated during sporulation. To elucidate if these SNP-specific gene expression variations had protein level changes and thereby directly affected phenotypic variation, we performed an absolute quantification of the yeast proteome in the sporulation medium for the four allele-specific strains (SS, MM, TT and MMTT). Since most of the SNP-specific gene expression changes were in early sporulation, we focussed on elucidating the early-phase proteome dynamics during sporulation, as differential expression patterns observed during this stage indicate genotype-driven phenotypic changes.

Employing absolute quantitative proteomics, we quantified proteins at two time points, once at an initial time point (0h) and during the early phase of sporulation (2h30m) (Figure 4A-B, Figure S5). Pearson correlation of 2996 pairs of transcripts (TPM) and protein abundance values (fmol/µg) for SS and MMTT strain showed a limited overall correlation between the datasets (correlation ranging between 0.393 – 0.461 and protein-mRNA slope represented as a regression line (depicts the relationship between the abundance of mRNA and the abundance of proteins) between 0.462-0.589 with p-value < 2.2e-15) (Figure 4C). These findings were consistent with previous findings in yeast[20,21] and human $CD8^+$ T cells[50].

Given this limited correlation, we analysed gene class-specific correlations. Genes were grouped based on the GO-slim mapper terms list, and their mRNA-protein slope and correlation were calculated. We observed that the ribosomal assembly, carbohydrate transport, carbohydrate metabolic process and monocarboxylic acid metabolic process show a higher slope and correlation than other gene classes (Figure 4D). Furthermore, our analysis revealed that the slope and correlation of gene class specific for respiration, meiotic cell cycle, amino acid transport, cellular amino acid metabolic process and sporulation were comparatively higher for the early phase of sporulation (2h30m) in both SS and MMTT strains compared to the initial timepoint (Figure 4D). These observations highlight that genes defined by the time point display distinct mRNA-protein correlations during sporulation.

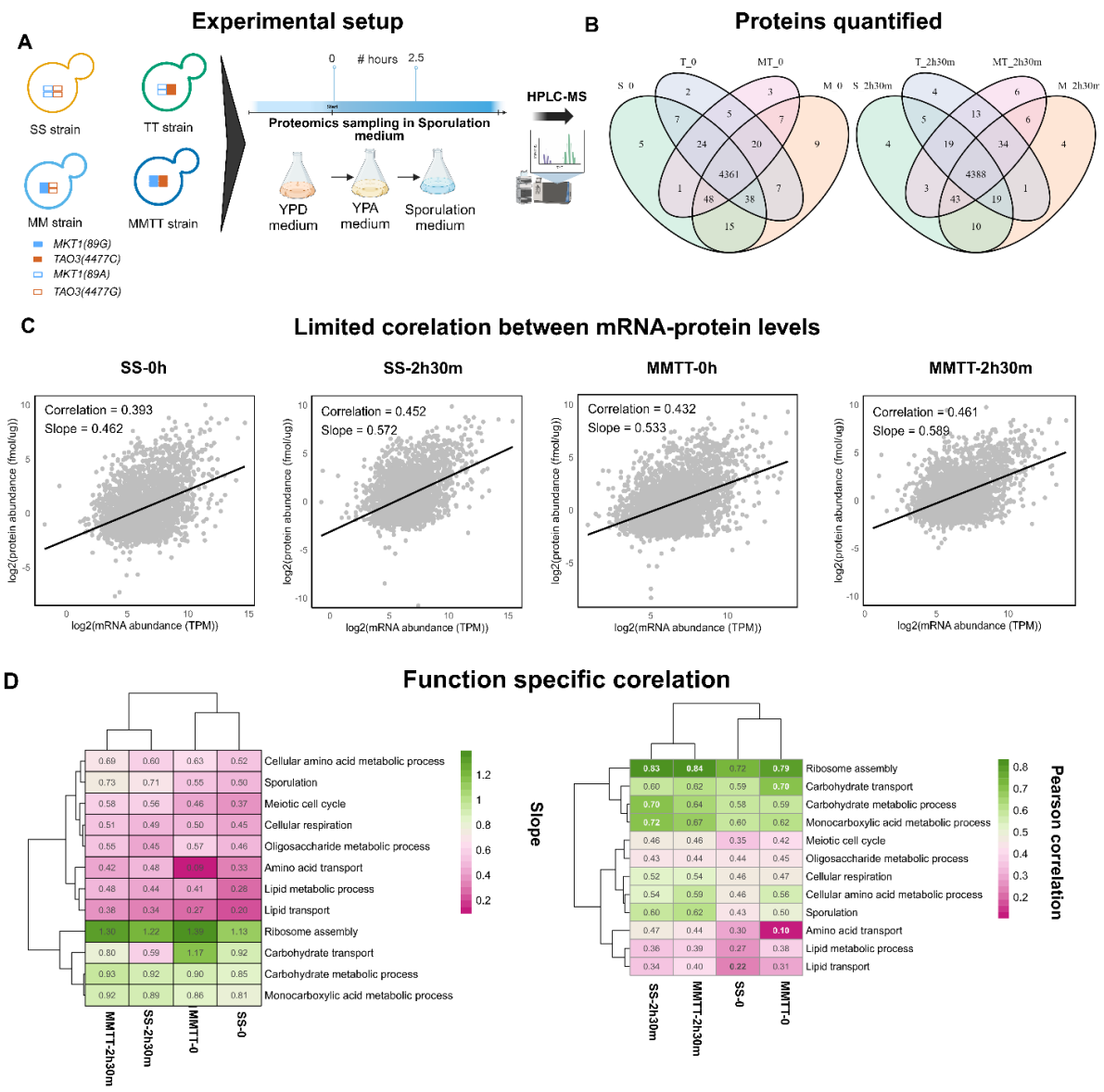

Figure 4: Experimental setup for absolute quantitative proteomics

(A) The S288c, MM, TT and MMTT strains were grown in the sporulation medium, and sampling was done at the 0th hour and 2h30m during sporulation. (B) Proteins were quantified at both time points for the four strains, with a substantial overlap. (C-D). The heatmap represents the correlation coefficients (E) and slope (F) of the integrated mRNA and protein abundance of various gene classes obtained for the Go-Slim mapper list.

Proteome allocation to arginine biosynthesis and mitochondrial respiration increases when *MKT1*^{89G} and *TAO3*^{4477C} genetically interact

The presence of causal variants can influence the protein expression changes and differentially activate pathways in response to genetic interactions between variants. To test this hypothesis, we first calculated the mass fraction of each protein and then conducted pairwise differential abundance analysis as described previously[51]. Differential protein abundance analysis revealed significant regulation of proteins across pairwise comparisons with the SS strain for respective time points (Table S6, S7). Specifically, at the 0h time point, we identified 123 proteins with significant regulation (105 upregulated and 18 down-regulated) when comparing the MM and SS strains. Similarly, when comparing the TT and SS strains, 26 proteins were significantly regulated (20 upregulated and six down-regulated). Notably, a substantial number of genes (206) were deregulated when comparing the MMTT and SS strains, with 188 upregulated and 16 downregulated proteins. Significant protein regulation was also evident during the early sporulation phase (2h30m). In the MM strain, we identified 65 regulated proteins (42 up, 23 down); in the TT strain, 35 proteins (13 up, 22 down); and in the MMTT strain, 98 proteins (86 up, 12 down) compared to the SS strain (Figure 5A). The upregulated proteins, both unique and shared among strains, are given in Table 1.

The gene ontology (GO)-term enrichment analysis revealed activated pathways or processes shared and unique between each SNP and their combination (Figure 5B). Cellular respiration and mitochondrial translation processes were enriched during 0h and 2h30m sporulation (Figure 5B) among the upregulated proteins in the MM and MMTT strains. This observation suggested a role for *MKT1*^{89G} in enhancing cellular respiration and mitochondrial activity during the early phases of sporulation. In contrast, no significant enrichment of gene ontology terms was observed for the TT strain.

Notably, we observed a unique enrichment of the arginine biosynthetic pathway exclusively for the MMTT strains at 0h and 2h30m (Figure 5B, 5C). We also observed mitochondrial genome maintenance, respiratory chain complex 3 assembly, and regulation of mitochondrial gene expression to be enriched uniquely to MMTT strain during the initiation of sporulation (Figure 5B).

The temporal changes in protein abundances were examined by comparing the 0h and 2h30m time points across all four strains (Figure S6A). The number of differentially expressed proteins at the 2h30m time point, in comparison to the 0h time point, showed that 7 proteins were found

to be upregulated in all strains at the 2h30m time point, including Ady2 (required for acetate utilisation during sporulation), Ino1, Cit3 (involved in the tricarboxylic acid cycle), Ena1 (expressed in response to glucose starvation), Pho89 (involved in phosphate metabolism), Leu1 (involved in leucine biosynthesis), Oac1 (oxaloacetate carrier), and Nce103 (necessary for the formation of bicarbonate, a step required for sporulation that increases the pH of the sporulation medium, Figure S6B, Table S8). Analysis of the downregulated proteins identified that in the MMTT strain specifically, several ribosomal proteins (Rtc6, Rpl22a, Rpl14b, Rpl4b, Rpl13a) were downregulated. This complemented our gene expression analysis, indicating that the MMTT strain reduces energy-intensive processes like ribosome biogenesis to promote sporulation.

Further, we investigated how proteome resources were reallocated in response to the causal variants and temporal progression in the sporulation medium. This approach provides a holistic view of how yeast strains adapt to nutrient-limited conditions by reallocating their cellular resources and helping to identify key proteomic adjustments that contribute to efficient sporulation. For this, we calculated the summed mass allocations of a group of proteins belonging to a particular GO term obtained from the yeast GO-slim mapper process terms dataset[51]. We then compared the SS and allele replacement strains (MM, TT, and MMTT) at each time point. We focused on GO terms that exhibited a significant p-value for at least one of the comparisons independently for each time point. We observed that 17 GO mapper processes were reallocated at 0h in response to causal variants (Figure S7A). At the same time, a substantial reallocation of proteins occurred during the 2h30 minute time, with 36 GO mapper processes being significantly reallocated (Figure S7B). At 0h, causal variants led to increased protein allocation to cellular respiration, as yeast cells had already been exposed to a pre-sporulation medium with acetate as the sole carbon source. We also noted a significant change in protein allocation to mitochondrial translation when the *MKT1*^{89G} variant was present. After 2h30m into sporulation, MM and MMTT strains showed significant enrichment for mitochondrial translation. Additionally, we found a unique enrichment of mitochondrial organisation and amino acid transport in the MMTT strain. In the case of the TT strain, we observed a significant protein allocation to the meiotic cell cycle and carbohydrate metabolic process.

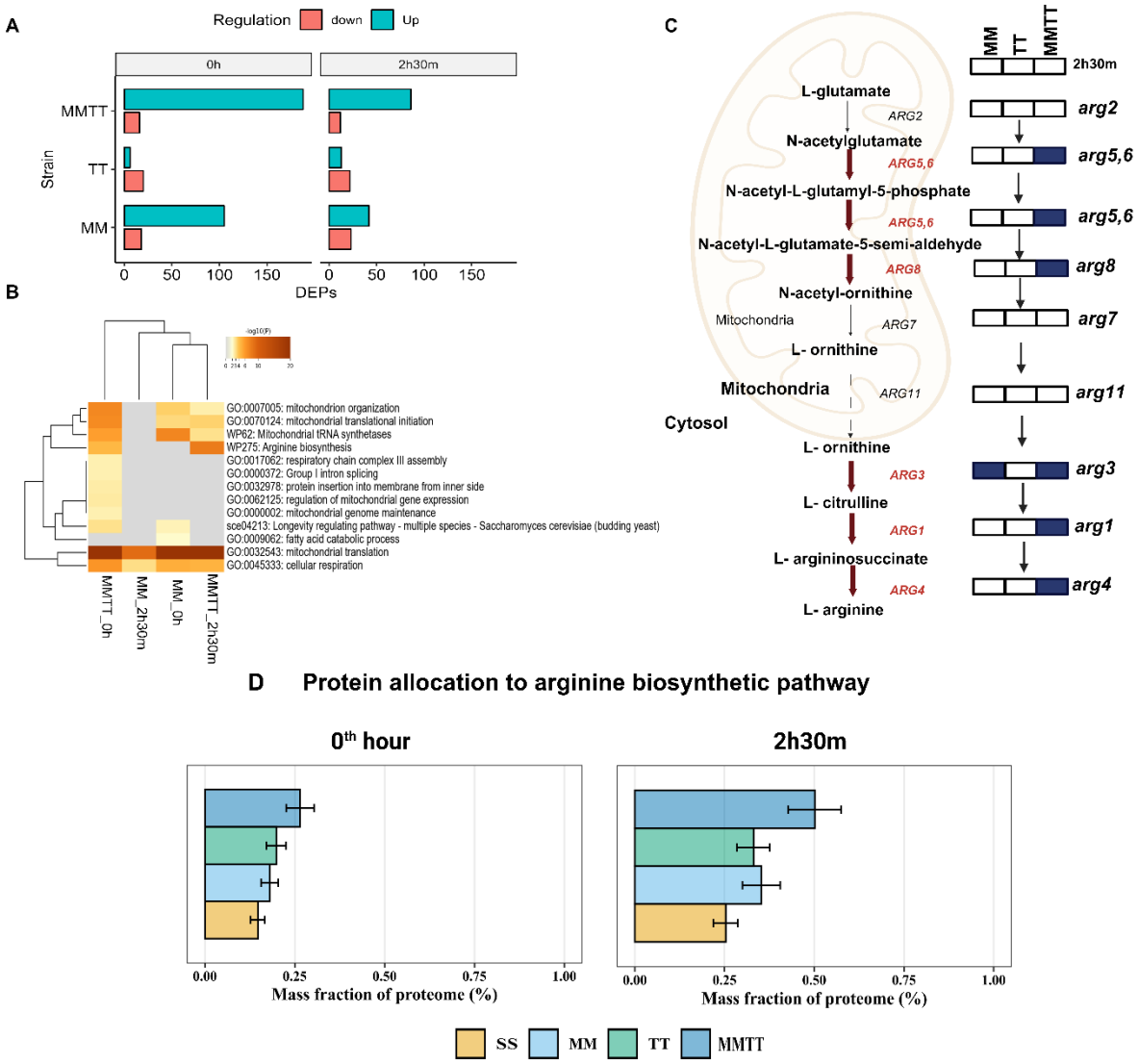

Figure 5: Differential enrichment of arginine biosynthetic pathway when *MKT1*^{89G} and *TAO3*^{4477C} interact

(A) Bar plots show the number of significantly expressed proteins compared with the S288c strain for the 0th hour and 2h30min. (B) GO enrichment analysis for upregulated genes in MM-0h, MM-2h30m, MMTT-0 and MTMT-2h30. The heatmap represents the p-value of each GO term clustered for both rows and columns. (C) Schematic representation of arginine biosynthetic pathway. The proteins represented in blue are differentially upregulated during 2h30m into sporulation (D) Allocation of the whole cellular proteome to arginine pathway in SS, MM, TT and MMTT during the 0th hour and early stage of sporulation (2h30m), calculated as the mean percentage allocation. Data are means ± SD of three biological replicates (except S-2h30m, which had two replicates).

As we identified an enrichment of upregulated proteins involved in the arginine biosynthetic process using differential protein abundance analysis, we wanted to examine how proteins are allocated to the arginine biosynthetic pathway. We found that the allocation to arginine metabolism increases during sporulation in all strains. Specifically, we found that the protein allocation to arginine metabolism in the MT strain was higher than in the SS, MM and TT strains during the 2h30min period (Figure 5D). We also observed that the protein is reallocated to amino acid metabolism from ribosomes and glycolysis during sporulation in a genotype-specific manner, suggesting yeast cells in nutrient-limited conditions redirect their protein resources towards amino acid metabolism rather than ribosomes, translation (Table 2), and glycolysis (Figure S8). This finding aligned with previous studies[51], demonstrating that yeast reallocated proteins to ribosomes in rich conditions, enhancing growth rates.

Functional validation of novel arginine biosynthetic pathway in modulating phenotypic additivity

From both transcriptomic and proteomic analyses, we have identified a distinctive regulation of the arginine biosynthetic process in the MMTT strain during the initial stages of sporulation. This discovery led us to hypothesise that this regulation could have a significant causal role in modulating sporulation efficiency, mainly through genetic interactions involving the $MKT1^{89G}$ and $TAO3^{4477C}$ SNPs. Previous studies on other yeast strains, such as SK1 and W303, known for their high sporulation efficiency, have shown an upregulation of the *ARG4* gene during early sporulation phases[34]. However, *arg4*Δ in the S288c strain, which typically exhibited lower sporulation efficiency, did not appear to affect the sporulation process. This phenotypic divergence among strains prompted us to investigate whether a unique interaction between the $MKT1^{89G}$ and $TAO3^{4477C}$ SNPs in the MT strain could modulate sporulation through the arginine biosynthesis pathway. To test this, deletions of *ARG4*, argininosuccinate lyase, a key enzyme involved in the final step of the arginine biosynthetic pathway and *ARG56*, acetyl glutamate kinase and N-acetyl-gamma-glutamyl-phosphate reductase catalysing the second and third step in arginine biosynthesis pathway, in SS, MM, TT, and MMTT strains were generated. Our working hypothesis was that if the arginine biosynthetic pathway served as a causal route responsible for the observed additive effects of the $MKT1^{89G}$ and $TAO3^{4477C}$ SNPs on sporulation efficiency, then the deletion of these key genes would have a more pronounced impact on the MMTT strain than on the other strains.

Sporulation efficiency of wildtype and deletion strains showed that *arg4*Δ and *arg56*Δ did not affect sporulation efficiency in SS, MM, and TT strains. In contrast, these deletions showed a sporulation deficit phenotype, specifically in the MMTT strain with *arg4*Δ, even after 48h in the sporulation medium (Figure 6A). This strain-specific phenotype suggested a potential link between *arg4*Δ and a defect in mitochondrial stability or respiration, crucial for the initiation of sporulation.

Since respiration is closely linked to the sporulation process, especially under nutrient-limiting conditions, we aimed to investigate the underlying respiratory dysfunction in the MT strain further. Growth phenotype of S, M, T, and MT strains and their *arg4*Δ in non-fermentable carbon sources, such as glycerol, ethanol, and glycerol/ethanol mixtures (YPG, YPE, and YPEG) showed that the S, M, and T strains showed no growth defects in these media. However, despite an extended incubation period of four days, MT-*arg4*Δ failed to grow in these non-fermentable carbon sources (Figure 6B). This indicates that *arg4*Δ in the MT strain shows a strong respiratory defect.

To find if the observed respiratory defect was linked to impaired mitochondrial activity, we performed a Mitotracker assay to measure mitochondrial activity in these strains. The assay was performed for 2h after transferring haploid cells to a non-fermentable carbon source (acetate). The Mitotracker assay results showed that the MT strain with *arg4*Δ significantly reduced mitochondrial activity compared to its wildtype (p-value < 0.001), indicating that *ARG4* was required to maintain mitochondrial function in the MT strain. In contrast, as expected, the S, M, and T strains did not show a reduction in mitochondrial activity following *arg4*Δ (Figure S9). We also measured mitochondrial activity in SS, MM, TT, and MMTT diploid strains after 2h of incubation in the sporulation medium. Consistent with the results from haploid cells, we found that only the MMTT strain with *arg4*Δ exhibited a pronounced reduction in Mitotracker intensity compared to the wildtype MMTT strain (Figure 6C). This suggested the essential role of *ARG4* in maintaining mitochondrial function, specifically in the MMTT strain. We also found that *arg4*Δ in the MMTT strain resulted in complete petite colonies, which suggests that *ARG4* is required to maintain mitochondrial stability (Figure 6D).

We then measured basal respiration rates in fermentable and non-fermentable media to further probe the effects of *arg4*Δ and *arg56*Δ on respiratory function. For this, we assessed the oxygen consumption rates (OCR) using a seahorse assay of all strains in acetate and glucose media, as

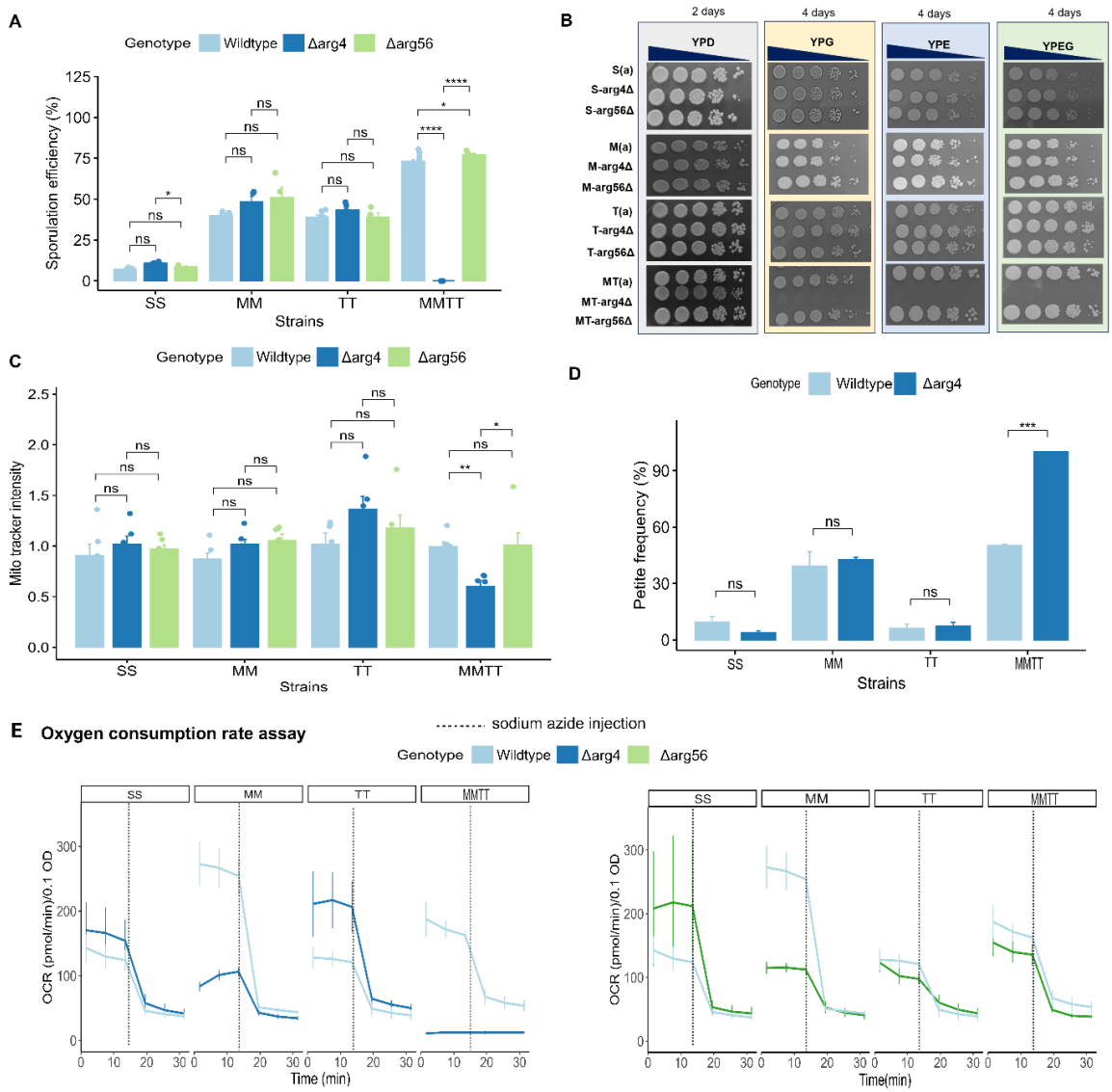

Figure 6: Functional validation of arginine pathway in bringing additive effect

(A) Sporulation efficiency calculated after 48h for wildtype (SS, MM, TT and MMTT) and their respective *arg4Δ and arg56Δ*. (B) 10-fold serial dilution of wildtype*, arg4Δ, arg56Δ* haploid strains of S288c, M, T and MT strains were spotted on YPD (2%), YPE (2%), YPG (2%) and YPEG. The pictures were taken after two days for YPD and four days for YPE, YPG and YPEG hours of incubation at 30˚C (C) Mito tracker intensity of diploid strains of SS, MM, TT and MMTT (wildtype and *arg4Δ*) after 2h incubation in sporulation medium (1% potassium acetate) (D) petite frequency assay of wildtype and *arg4Δ* of MMTT strain. (E) The oxygen consumption rate (OCR) of SS, MM, TT and MMTT for WT (n = 4), *arg4Δ* (n = 4) and *arg5Δ* (n = 3) cells were measured using the Seahorse Extracellular Flux 96 Analyzer grown in acetate media. After three basal measurements, sodium azide was injected into the wells to shut off mitochondrial oxygen consumption, and an additional three sets of measurements were taken.

P-values were calculated using an unpaired t-test in the rstatix R package (v.0.7.2). Significance levels are indicated as follows: **** p < 1e-4, *** p < 1e-3, ** p < 1e-2, * p < 5e-2, and ns (not significant) for p > 5e-2. The mean ± s.e. of at least three biological replicates is shown.

acetate is known to be a respiratory substrate. The results revealed that neither *arg4*Δ nor *arg56*Δ significantly impacted OCR in the SS and TT strains, indicating that respiration in these strains remains unaffected mainly by disruptions in the arginine biosynthetic pathway (Figure 6D). However, in the MM strain, both deletions led to a reduction in OCR, though this reduction did not impair sporulation efficiency, suggesting that compensatory mechanisms support sporulation independently of respiration. Only in the MMTT strain did *arg4*Δ completely abolish respiratory function, while *arg56*Δ had no significant effect on respiration (Figure 6D). Interestingly, these patterns were not observed when glucose was used as the carbon source, highlighting the respiratory-specific impact of *arg4*Δ (Figure S10).

In conclusion, our findings demonstrated that the arginine biosynthesis pathway was critical in initiating sporulation and maintaining mitochondrial function in the MMTT strain. The genetic interaction between the $MKT1^{89G}$ and $TAO3^{4477C}$ SNPs modulated this pathway, linking mitochondrial activity and respiration to the sporulation process, specifically in the MMTT strain.

DISCUSSION

Genome-wide gene deletion studies have shown that the combination of gene deletions can be additive, and epistatic interactions have different phenotypic effects than the effect of individual gene deletions[6,52,53]. This study shows that when two additive effect SNPs are present together in a strain, they impact the phenotype by activating a novel metabolic pathway different from the metabolic pathways of individual SNP effects. Our result has consequences for understanding how variants affect disease phenotypes, specifically in complex traits where multiple SNP combinations can have differential outcomes in the progression of the disease and treatment responses.

Using multi-omics approaches, we combined temporal transcriptome and proteome profiling of isogenic yeast strains, and we were able to ascertain that the strain with combined SNPs, $MKT1^{89G}$ and $TAO3^{4477C}$, activated the amino acid metabolism pathways early in sporulation while simultaneously downregulating ribosome-related processes. This observation suggested

a metabolic trade-off wherein yeast reduces energy-intensive processes like ribosome biogenesis and redirects resources toward amino acid biosynthesis in response to nutrient starvation[54]. The enrichment of GO terms related to mitochondrial gene expression, organisation, and translation initiation points to a substantial reprogramming of the mitochondrial network and its biogenesis machinery during the early stages of adaptation to respiratory metabolism. These findings are consistent with previous reports by Björkeroth et al.[51]. We also found that the strains with both SNPs in combination can activate the arginine biosynthetic pathway differentially by allocating more protein to arginine biosynthesis than to ribosome biogenesis and glycolysis. Further, through experimental validation, we have shown that *ARG4* is necessary to maintain mitochondrial activity and respiration only when $MKT1^{89G}$ and $TAO3^{4477C}$ SNPs are combined. We speculate that due to the genetic interactions between $MKT1^{89G}$ and $TAO3^{4477C}$ SNPs, a rewiring of the metabolic network makes mitochondrial function heavily dependent on the arginine biosynthetic pathway.

Our results show that, in yeast, particular SNP-SNP interactions can substantially impact the control of critical metabolic pathways that reroute amino-acid production during sporulation and shut down ribosome biogenesis. These findings provide compelling evidence that genetic interactions can precisely tune cellular responses to suit physiological requirements and environmental inputs. The findings raise whether these insights and mechanisms can be extrapolated to human diseases, particularly cancer. Cancer is the opposite of yeast sporulation, which is characterised by uncontrolled and excessive cell proliferation driven by the hyperactivation of growth-related pathways, including ribosome biogenesis and metabolic processes[55,56]. As we observed in our yeast model, where SNP-SNP combinations regulated a metabolic trade-off in sporulation, certain SNP combinations in cancer might likely hyperactivate ribosomal pathways while simultaneously shutting down other metabolic pathways that normally control growth. Identifying and understanding these SNP-SNP dependencies could definitively reveal gene-gene interactions that either promote or suppress cancer progression. Targeting these genetic interactions could offer new therapeutic intervention possibilities. For instance, by identifying SNP combinations that promote these metabolic trade-offs in cancer, specific drugs targeting these interactions can inhibit the excessive proliferation of cancer cells while minimising the impact on normal, healthy cells.

MATERIALS AND METHODS

Allele replacement strains

All yeast strains are derivatives of S288c, a widely used laboratory strain, and their relevant genotypes are listed in Table S1. The available diploid MM strain with *MKT1*^{89G} allele and TT strain with *TAO3*^{4477C} allele, corrected for background mutations, were validated for their SNPs using allele-specific PCRs and Sanger sequencing. The haploids of M and T strains were generated by sporulating their respective diploid strains, followed by spore enrichment. The resulting M and T haploids were confirmed using MAT locus PCR. The opposite mating types of M and T strains were crossed to obtain the diploid MsTs strain with genotype *MKT1*^{89G}/*MKT1*^{89A} *TAO3*^{4477C}/*TAO3*^{4477G}. The diploid MsTs strain was sporulated and spore enriched which resulted in segregants having all possible combinations of *MKT1* and *TAO3* alleles: Mt (*MKT1*^{89G}/*TAO3*^{4477G}), mt (*MKT1*^{89A}/*TAO3*^{4477G}), mT (*MKT1*^{89A}/*TAO3*^{4477C}), and MT (*MKT1*^{89G}/*TAO3*^{4477C}). The MT haploids were selected by performing allele-specific PCRs and were further validated using Sanger sequencing. The opposite mating types of MT haploids were mated to obtain the diploid MMTT strain with genotype *MKT1*^{89G}/*MKT1*^{89G} *TAO3*^{4477C}/*TAO3*^{4477C}. All further experiments are performed using the diploid MMTT strain.

Phenotyping for sporulation efficiency

The diploid SS, MM, TT and MsTs, SK1, and MMTT strains were phenotyped for sporulation efficiency. Briefly, the strains were first grown in YPD (2% (w/v) yeast extract, 1% (w/v) peptone, 2% (w/v) dextrose) from OD 0.2 to 1.0 and then grown in YPA (1% (w/v) yeast extract, 2% (w/v) peptone, 1% (w/v) potassium acetate from OD 0.2 to 1.0. The cells were washed in water, then in potassium acetate, and then incubated in 1% potassium acetate supplemented with amino acids. The sporulation efficiency was calculated as the ratio of dyads and tetrads produced by a strain to the number of single nucleus cells.

Generation of *ARG4 and ARG56* deletion mutants

The gene deletions of *ARG4* and *ARG56* were performed in haploids of S, M, T and MT by replacing the *ARG4* and *ARG56* genes with drug resistance cassettes (hphMX4) by following high-efficiency lithium acetate protocol[57]. The transformants were selected by plating onto YPD media containing hygromycin. The deletion confirmation (homologous integration) was done by colony PCR of insertion junctions using junction-specific primers. The deletion confirmed haploid cells were diploidised by transforming strains with pHS03 plasmid (resistant

to Nat) and confirmed using MAT locus PCR. The list of primers used in this study is given in Table S2. Further, the diploid strains with respective deletions were phenotyped for sporulation efficiency and for studying mitochondrial activity.

Spot dilution assay

Overnight cultures of the strains were grown in 5 mL of YPD and diluted to an A600 of 1. Ten-fold serial dilutions were prepared, and 5 µL of each dilution was spotted onto fermentable media (YPD) and respiratory media (YPGlycerol (2%), YPEthanol (2%), YPEG (1% ethanol +3% glycerol)). The final A600 values of the spots were 1, 0.1, 0.01, 0.001, and 0.0001. Plates were incubated at 30°C, with growth captured after 2 days for YPD and 4 days for the respiratory media.

Mitotracker fluorescence assay

The Mitotracker plate reader assay was adapted from Vengayil et al.[58] with modifications for high-throughput analysis. In brief, overnight yeast cultures were initially grown in YPD medium, followed by secondary cultures diluted to an OD600 of 0.2 and grown to an OD600 of 1.0. Cells were washed and incubated in 1% potassium acetate for 2h. Following this, Mitotracker was added to each well to a final concentration of 200 nM, and the plates were incubated in the dark for 30m at 30°C in a shaking incubator. After incubation, the plates were centrifuged at 1,700 rpm for 2min, and the supernatant was discarded. The cells were washed once with PBS (pH 7.4) to remove excess dye and media, and 200 µL of PBS was added to each well. The cells were resuspended and transferred to black plates for fluorescence measurement. Fluorescence was recorded using a multimode plate reader at excitation/emission wavelengths of 572/599 nm. Finally, the fluorescence signal was normalised using the optical density (OD_{600}) of the same samples, which was measured.

Petite frequency assay

Three independent colonies were resuspended in 1 mL of PBS, diluted, and plated on YPDG medium (1% yeast extract, 2% peptone, 0.1% glucose, and 3% glycerol) to yield approximately 200-400 colonies per plate. After five days of incubation, colonies were counted, distinguishing between large colonies (grande) and small colonies (petite). The petite frequency was calculated as the ratio of petite colonies to the total number of colonies per plate. Petite colonies were further validated by patching them onto YPE plates to confirm their inability to grow on this medium.

Oxygen consumption rate assay

Yeast oxygen consumption rate (OCR) measurements were performed using the Agilent Seahorse XF Pro analyser, following a protocol specifically optimised for 0.5% sodium azide injection, as outlined in[59,60]. On the first day, overnight yeast cultures (consisting of 4 biological replicates each for SS, MM, TT, and MMTT and four biological replicates for *arg4* deletion strains and three biological replicates for *ARG5* deletion strains) were prepared. The Seahorse XF96 sensor cartridge was pre-incubated with 200 µl of calibrant solution per well at 30°C in a CO_2-free incubator. The Seahorse assay media containing glucose and acetate (0.167% yeast nitrogen base, 0.5% ammonium sulphate, and 1% acetate or 2% dextrose, respectively) was prepared. The microplate wells were coated with 60 µl of poly-L-lysine (0.1 mg/ml), incubated for 1h, washed twice with PBS, and stored at room temperature overnight. On the second day, overnight yeast cultures grown in YPD were diluted and grown until reaching an OD_{600} of 0.5-0.7 (mid-log phase). The cells were washed and diluted to a specific concentration in Seahorse assay media (glucose or acetate). The cells were seeded into poly-L-lysine-treated wells of the XF96 microplate, then centrifuged at 500 rpm for 5min and incubated at 30°C for 1h. The sensor cartridge was loaded with 0.5% sodium azide in chamber A and was calibrated. Three basal OCR measurements were recorded at 30°C for 3min each, with 2min of mixing between readings. Following the injection of 0.5% sodium azide into chamber A, three additional OCR measurements were taken, following the same procedure. The measured OCR values were then normalised to OD 0.1.

Temporal transcriptome profiling, data pre-processing and removing outlier samples

The SS and MMTT strains were first grown in YPD and then in YPA and transferred to the sporulation medium (1% potassium acetate and amino acid supplements). The samples were taken at 0h, 30min, 45min, 1h10min, 1h40min, 2h30min, 3h50min, 5h40min, and 8h30min and were snap frozen and stored at -80 degree. RNA extraction, quality control, library preparation, and paired-end sequencing using Illumina Novaseq were conducted by an external service provider (Genotypic Technology, Bangalore, India). The detailed protocols followed for RNA isolation and library preparation are discussed in the Supplementary Methods section.

The raw Fastq files were given as input to a customised Snake make pipeline, which performs quality checks using FASTQC and MutiQC[61], removes rRNA contamination, performs alignment using STAR[62], and finally gives the feature counts as output. The feature count file was then provided as input to the IDEP 2.0 software[63] for initial quality checks. The low counts

were filtered such that three counts per million (edge R) were in at least three samples. Thus, 6207 genes from an initial list of 7127 genes were selected for further analysis. Using the 300 most variable genes, hierarchal clustering and PCA were performed for all 54 samples, which removed five potential outlier samples from further analysis.

Differential expression analysis using DESeq2 in IDEP software

Initially, we aimed to independently identify genes exhibiting significant differential expression relative to the baseline (0th hour) at each time point for both SS and MMTT strains. Our dataset comprised 24 samples for the MMTT strain, encompassing 7,127 genes. Subsequently, we filtered this dataset to retain 6,447 genes with a minimum count per million (CPM) threshold of 0.5 across at least three samples. Employing the DESeq2[48] algorithm with a false discovery rate (FDR) cutoff of 0.05 and a minimum fold change of 2, along with the Wald test and independent filtering, we identified genes showing significant differential expression. Similarly, in the S strain, we analysed a dataset containing 6409 genes that passed the aforementioned filtering criteria. We used DESeq2 under identical parameters to identify genes exhibiting differential expression relative to the 0th hour time point.

Temporal differential expression analysis using Likelihood Ratio Test (LRT) method

We further investigated temporal differential gene expression employing the LRT method within DESeq2. This approach evaluates whether significant differences in genotype effects exist across various time points. To construct the 'full model,' we integrated key sources of variation, including genotype and time, along with our condition of interest, i.e., the interaction between genotype and time (genotype: time). By contrasting this full model with a 'reduced model' lacking the genotype: time term, we identified genes exhibiting significant alterations in expression profiles between SS and MMTT strains across multiple time points. This analysis enabled us to pinpoint genes whose expression trajectories were influenced by the presence of $MKT1^{89G}$ and $TAO3^{4477C}$.

Temporal gene expression clustering using DPGP

For our analysis, we utilised gene expression data normalised to Transcripts Per Million (TPM) and provided them as input to the DPGP algorithm[49]. To optimise computational efficiency, we employed the --fast option, which utilises an accelerated computation mode. Moreover, we utilised the --true_times parameter to preserve the temporal information associated with each

expression profile during the clustering process. This enabled us to capture the temporal dynamics inherent in the data accurately.

Extracellular metabolite analysis

Three biological replicates of SS, MM, TT and MMTT strains were grown in YPD, followed by growth in YPA and then transferred to 1% potassium acetate as described previously. Samples (OD = 1.0) in sporulation medium were collected at appropriate time points, and the extracellular medium was filtered using 0.45 µm filters and stored at -20°C until analysis. Extracellular acetate levels in the sporulation medium were measured using high-performance liquid chromatography (HPLC) equipped with a Bio-Rad HPX-87H column and an infrared detector. The elution buffer used was 9 mM H_2SO_4, with a flow rate of 0.7 mL/min, and the column was maintained at an oven temperature of 60°C.

Absolute quantitative proteomics using mass spectrometry

To capture the absolute proteome changes during the initial phases of sporulation, where *MKT1*^{89G} and *TAO3*^{4477C} *SNPs* were found to be active, we performed absolute proteomics experiments for all four strains at two time points. For this, 4 ml (OD = 1.0) of the diploid strains SS, MM, TT and MMTT sampled at 0th and 2h30min after incubation in sporulation medium as described was centrifuged for 2min at 4degree at 4000g, the supernatant was discarded, and cell pellets were snap frozen in dry ice and kept in -60-degree freezer until further analysis.

Sample preparation for proteomics analysis was performed as described previously by Kozaeva et al.[64], and any modifications are mentioned below. Cell pellets of *S. cerevisiae* were lysed in 6 M guanidinium·HCl, 5 M tris(2-carboxyethyl) phosphine, 10 M chloroacetamide and 100 M Tris·HCl (pH = 8.5), disrupted mechanically and heated to 99°C. After centrifugation, the cell-free lysates were diluted with 50 M ammonium bicarbonate and subjected to a bicinchoninic acid (BCA) assay to estimate protein concentrations. Trypsin and LysC digestion mix (Promega) was added to 20 µg protein of each sample and incubated for 8 hours. Trifluoroacetic acid was added to halt digestion, and the samples were desalted using C18 resin (Empore, 3M) before HPLC-MS analysis. HPLC-MS analysis of the samples was performed on an Orbitrap Exploris 480 instrument (Thermo Fisher Scientific), preceded by an EASY-nLC 1200 HPLC system (Thermo Fisher Scientific). For each sample, 0.5 µg of peptides were captured on a 2 cm C18 trap column (Thermo Fisher 164946). Subsequently, separation was executed using a 70 min gradient from 8% (v/v) to 48% (v/v) of acetonitrile in 0.1% (v/v)

formic acid on a 15 cm C18 reverse-phase analytical column (Thermo EasySpray ES904) at a flow rate of 250 nL/min. For data-independent acquisition, the mass spectrometer was run with the HRMS1 method as previously described[65], preceded by the FAIMS Pro Interface (Thermo Fisher Scientific) with a compensation voltage (CV) of -45 V, and any modifications are mentioned below. Full MS1 spectra were collected at a resolution of 120,000 and a scan range of 400-1,000 m/z, with the maximum injection time set to auto. MS2 spectra were obtained at a resolution of 60,000, with the maximum injection time set to auto and the collision energy set to 32. Each cycle consisted of three DIA experiments, each covering a range of 200 m/z with a window size of 6 m/z and a 1 m/z overlap, while a full MS scan was obtained between experiments.

Processing of Mass Spectrometric Raw Data

Sequence identification was performed for all analyses using a protein database consisting of the *S. cerevisiae* S288c (UP000002311; accessed on the 17th of November 2023) reference proteome. Spectronaut V18 was used for protein identification and relative quantification of peptides for DIA data analysis. The default settings for "directDIA" were applied with an FDR cut-off of 1%, except for MS1 quantification for the peptides. Protein abundances were inferred from the peptide abundances using the xTop algorithm[66]. Absolute protein quantification was performed through the TPA (total protein approach)[67] method to the final units of fmol per µg total protein as proteome composition values.

Differential protein expression and allocation analysis

We converted the fmol per µg total protein to the percentage of the entire protein mass (g per µg total protein). This was done by multiplying by molecular weight and dividing by the sum of all proteins. This analysis expressed every protein abundance as a percentage of the entire proteomic mass. These mass percentages were then used for subsequent protein allocation and differential abundance analysis. For GO-slim mapper process terms analysis, all proteins in all datasets were merged, and the terms that matched the proteins were annotated to them as described in Björkeroth et al.[51]. For the summation of allocation, each dataset was subsequently matched to the set-up GO-slim mapper process term framework to identify which proteins are to be summed. The differential expression of proteins between wildtype (SS) vs allele replacement strains (MM, TT and MMTT) and also between the time points (0h vs 2h30m) were performed using the log2-transformed values with unpaired two-sided Student's t-test.

The significantly reallocated proteins are proteins with a $\log_2$(fold change) greater than 1 or less than -1 and a P value < 0.05 for all pairwise comparisons performed using the dataset.

mRNA-protein correlation analysis

To understand how mRNA correlates with the protein levels, we computed the Pearson correlation, plotting the average $\log_2$(TPM) for mRNA against the average $\log_2$(abundance) protein. The cor.test() function from the R 'stats' package was employed to assess the statistical significance of correlations. Further, the mRNA-protein slope was identified from the coefficient derived from the linear model (lm() function in R's 'stats' package) using the formula 'lm(protein ~ mRNA)', where 'protein' is the $\log_2$(abundance) and 'mRNA' is the $\log_2$(TPM).

Generation and analysis of context-specific models

We employed a genome-scale metabolic modelling approach to understand how the SNPs and their interactions can influence the intracellular flux variation during the early sporulation phase. We generated context-specific metabolic models by Integrating the protein expression data with the yeast genome-scale metabolic model (Yeast9)[68]. Further, we analysed the intracellular flux variation between the generated models using genome-scale differential flux analysis (GS-DFA) as described in the Supplementary Methods section.

ACKNOWLEDGMENTS

We thank Veerendra Gadekar, IIT Madras, for his assistance in setting up the initial RNAseq preprocessing pipeline and discussions, and Divya, DTU, for her assistance with HPLC. Additionally, SrS received HTRA from IIT Madras and a travel fellowship from IBSE, IIT Madras.

FUNDING

We acknowledge core funding to IBSE, IIT Madras (BIO/1819/304/ALUM/KARH) and the Center of Excellence funding to IBSE (SB/2021/0841/BT/MHRD/08752). For cultivation, HPLC and proteome analysis, we acknowledge the funding received from The Novo Nordisk Foundation (NNF20CC0035580).

DATA, MATERIALS, AND CODE AVAILABILITY

Fastq files and raw gene-count data tables are available on GEO under the accession number GSE278261. The mass spectrometry proteomics data have been deposited to the

ProteomeXchange Consortium via the PRIDE[69] partner repository with the dataset identifier PXD056947. The R codes used for analyses are available on Zenodo (https://doi.org/10.5281/zenodo.13917859)[70]

AUTHOR CONTRIBUTIONS

SrS generated strains, analysed RNAseq and protein abundance data, developed GSMM modelling, performed validation experiments, and wrote the first draft; STP performed proteomics experiments and analysed mass spectrometry data; SS, HS, conceptualisation, supervision, and funding acquisition; SrS, HS wrote the manuscript; all authors edited and finalised the manuscript.

DECLARATION OF INTEREST

The authors declare no competing interests.

REFERENCES

1. Mackay TFC, et al. The genetics of quantitative traits: challenges and prospects. *Nat Rev Genet*. 2009;10(8):565-577. doi:10.1038/nrg2612
2. Lappalainen T, et al. Genetic and molecular architecture of complex traits. *Cell*. 2024;187(5):1059-1075. doi:10.1016/j.cell.2024.01.023
3. Gerke J, et al. Genetic interactions between transcription factors cause natural variation in yeast. *Science*. 2009;323(5913):498-501. doi:10.1126/science.1166426
4. Bloom J, et al. Genetic interactions contribute less than additive effects to quantitative trait variation in yeast. *Nat Commun*. 2015;6:8712. https://doi.org/10.1038/ncomms9712
5. Hale JJ, et al. Genome-scale analysis of interactions between genetic perturbations and natural variation. *Nat Commun*. 2024;15(1):4234. doi:10.1038/s41467-024-48626-1
6. Costanzo M, et al. A global genetic interaction network maps a wiring diagram of cellular function. *Science*.2016;353(6306):aaf1420. doi:10.1126/science.aaf1420
7. Forsberg SKG, et al. Accounting for genetic interactions improves modeling of individual quantitative trait phenotypes in yeast. *Nat Genet*. 2017;49(4):497-503. doi:10.1038/ng.3800
8. Matsui T, et al. The interplay of additivity, dominance, and epistasis on fitness in a diploid yeast cross. *Nat Commun*. 2022;13(1):1463. doi:10.1038/s41467-022-29111-z
9. Cordell HJ. Detecting gene-gene interactions that underlie human diseases. *Nat Rev Genet*. 2009;10(6):392-404. doi:10.1038/nrg2579
10. Webber C. Epistasis in Neuropsychiatric Disorders. *Trends Genet*. 2017;33(4):256-265. doi:10.1016/j.tig.2017.01.009
11. Abegaz F, et al. Epistasis detection in genome-wide screening for complex human diseases in structured populations. *Syst Med*. 2019;2(1):19-27. doi:10.1089/sysm.2019.0003
12. Li Y, et al. Statistical and functional studies identify epistasis of cardiovascular risk genomic variants from genome-wide association studies. *J Am Heart Assoc*. 2020;9(7):e014146. doi:10.1161/JAHA.119.014146

13. Fang G, et al. Discovering genetic interactions bridging pathways in genome-wide association studies. *Nat Commun*. 2019;10(1):4274. doi: 10.1038/s41467-019-12131-7

14. Shalem O, et al. Genome-scale CRISPR-Cas9 knockout screening in human cells. *Science*. 2014;343(6166):84-87. doi:10.1126/science.1247005

15. Yadav A, et al. Differential regulation of cryptic genetic variation shapes the genetic interactome underlying complex traits. *Genome Biol Evol*. 2016;8(12):3559-3573. doi:10.1093/gbe/evw258

16. Visscher PM, et al. 10 years of GWAS discovery: biology, function, and translation. *Am J Hum Genet*. 2017;101(1):5-22. doi:10.1016/j.ajhg.2017.06.005

17. Cano-Gamez E, Trynka G. From GWAS to function : using functional genomics to identify the mechanisms underlying complex diseases. 2020;11:1-21.

18. Mullis MN, et al. The complex underpinnings of genetic background effects. *Nat Commun*. 2018;9(1):3548. doi: 10.1038/s41467-018-06023-5

19. Chandler CH, et al. Causes and consequences of genetic background effects illuminated by integrative genomic analysis. *Genetics*. 2014;196(4):1321-1336. doi:10.1534/genetics.113.159426

20. Xia J, et al. Proteome allocations change linearly with the specific growth rate of *Saccharomyces cerevisiae* under glucose limitation. *Nat Commun*. 2022;13(1):2819. doi:10.1038/s41467-022-30513-2

21. Yu R, et al. Quantifying absolute gene expression profiles reveals distinct regulation of central carbon metabolism genes in yeast. *Elife*. 2021;10. doi:10.7554/eLife.65722

22. Bar-Joseph Z, et al. Studying and modelling dynamic biological processes using time-series gene expression data. *Nat Rev Genet*. 2012;13(8):552-64. doi: 10.1038/nrg3244

23. Liti G, Louis EJ. Advances in quantitative trait analysis in yeast. *PLoS Genet*. 2012;8(8):e1002912. doi:10.1371/journal.pgen.1002912

24. Deutschbauer AM, Davis RW. Quantitative trait loci mapped to single-nucleotide resolution in yeast. *Nat Genet*. 2005;37(12):1333-40. doi: 10.1038/ng1674

25. Civelek M, Lusis AJ. Systems genetics approaches to understand complex traits. *Nat Rev Genet*. 2014;15(1):34-48. doi:10.1038/nrg3575

26. Chen C, et al. Applications of multi-omics analysis in human diseases. *MedComm*. 2023;4(4):e315. doi:10.1002/mco2.315

27. Kreitmaier P, et al. Insights from multi-omics integration in complex disease primary tissues. *Trends Genet*. 2023;39(1):46-58. doi:10.1016/j.tig.2022.08.005

28. Wigger L, et al. Multi-omics profiling of living human pancreatic islet donors reveals heterogeneous beta cell trajectories towards type 2 diabetes. *Nat Metab*. 2021;3(7):1017-1031. doi:10.1038/s42255-021-00420-9

29. Wang P, et al. Prediction of plant complex traits via integration of multi-omics data. *Nat Commun*. 2024;15(1):6856. doi:10.1038/s41467-024-50701-6

30. Aleksandrova K, et al. Omics biomarkers in obesity: Novel etiological insights and targets for precision prevention. *Curr Obes Rep*. 2020;9(3):219-230. doi:10.1007/s13679-020-00393-y

31. Doran S, et al. Multi-omics approaches for revealing the complexity of cardiovascular disease. *Brief Bioinform*. 2021;22(5). doi:10.1093/bib/bbab061

32. Migliozzi S, et al. Integrative multi-omics networks identify PKCδ and DNA-PK as master kinases of glioblastoma subtypes and guide targeted cancer therapy. *Nat Cancer*. 2023;4(2):181-202. doi:10.1038/s43018-022-00510-x

33. Liang XJ, et al. Advances in multi-omics study of prognostic biomarkers of diffuse large B-cell lymphoma. *Int J Biol Sci*. 2022;18(4):1313-1327. doi:10.7150/ijbs.67892

34. Primig M, et al. The core meiotic transcriptome in budding yeasts. *Nat Genet*. 2000;26(4):415-23. doi:10.1038/82539

35. Kassir Y, et al. Transcriptional regulation of meiosis in budding yeast. *Int Rev Cytol*. 2003;224:111-71. doi:10.1016/s0074-7696(05)24004-4

36. Francesconi M, Lehner B. The effects of genetic variation on gene expression dynamics during development. *Nature*. 2014;505(7482):208-11. doi:10.1038/nature12772

37. Becker K, et al. Quantifying post-transcriptional regulation in the development of *Drosophila melanogaster*. *Nat Commun*. 2018;9(1):4970. doi:10.1038/s41467-018-07455-9

38. Ridder M den, et al. Proteome dynamics during transition from exponential to stationary phase under aerobic and anaerobic conditions in yeast. *Mol Cell Proteomics*. 2023;22(6):100552. doi:10.1016/j.mcpro.2023.100552

39. Gupta S, et al. Temporal expression profiling identifies pathways mediating effect of causal variant on phenotype. *PLoS Genet*. 2015;11(6):e1005195. doi:10.1371/journal.pgen.1005195

40. Gupta S, et al. Meiotic interactors of a mitotic gene *TAO3* revealed by functional analysis of its rare variant. *G3 (Bethesda)*. 2016;6(8):2255-2263. doi:10.1534/g3.116.029900

41. Arakelyan A, et al. Temporal changes of gene expression in health, schizophrenia, bipolar disorder, and major depressive disorder. *Schizophrenia (Heidelb)*. 2024;10(1):19. doi:10.1038/s41537-024-00443-7

42. Sudarsanam P, Cohen BA. Single nucleotide variants in transcription factors associate more tightly with phenotype than with gene expression. *PLoS Genet*. 2014;10(5):e1004325. doi:10.1371/journal.pgen.1004325

43. Sasikumar S, et al. Genome-scale metabolic modeling identifies causal reactions mediated by SNP-SNP interactions influencing yeast sporulation. *bioRxiv*. Published online 15 September 2023. doi:10.1101/2023.09.13.557398

44. Neiman AM. Sporulation in the budding yeast *Saccharomyces cerevisiae*. *Genetics*. 2011;189(3):737-765. doi:10.1534/genetics.111.127126

45. Enyenihi AH, Saunders WS. Large-scale functional genomic analysis of sporulation and meiosis in Saccharomyces cerevisiae. *Genetics*. 2003;163(1):47-54. doi:10.1093/genetics/163.1.47

46. Deutschbauer AM, et al. Parallel phenotypic analysis of sporulation and postgermination growth in *Saccharomyces cerevisiae*. *Proc Natl Acad Sci U S A*. 2002;99(24):15530-15535. doi:10.1073/pnas.202604399

47. Tomar P, et al. Sporulation genes associated with sporulation efficiency in natural isolates of yeast. *PLoS One*. 2013;8(7):e69765. doi:10.1371/journal.pone.0069765

48. Love MI, et al. Moderated estimation of fold change and dispersion for RNA-seq data with DESeq2. *Genome Biol*. 2014;15(12):550. doi: 10.1186/s13059-014-0550-8

49. McDowell IC, et al. Clustering gene expression time series data using an infinite Gaussian process mixture model. *PLoS Comput Biol*. 2018;14(1):e1005896. doi:10.1371/journal.pcbi.1005896

50. Nicolet BP, Wolkers MC. The relationship of mRNA with protein expression in CD8+ T cells associates with gene class and gene characteristics. *PLoS One*. 2022;17(10):e0276294. doi: 10.1371/journal.pone.0276294

51. Björkeroth J, et al. Proteome reallocation from amino acid biosynthesis to ribosomes enables yeast to grow faster in rich media. *Proc Natl Acad Sci U S A*. 2020;117(35):21804-21812. doi:10.1073/pnas.1921890117

52. Costanzo M, et al. Global genetic networks and the genotype-to-phenotype relationship. *Cell*. 2019;177(1):85-100. doi:10.1016/j.cell.2019.01.033

53. Costanzo M, et al. Environmental robustness of the global yeast genetic interaction network. *Science*. 2021;372(6542):eabf8424. doi:10.1126/science.abf8424

54. Shore D, Albert B. Ribosome biogenesis and the cellular energy economy. *Curr Biol*. 2022;32(12):R611-R617. doi:10.1016/j.cub.2022.04.083

55. Piazzi M, et al. Signal transduction in ribosome biogenesis: a recipe to avoid disaster. *Int J Mol Sci*. 2019;20(11):2718. doi:10.3390/ijms20112718

56. Elhamamsy AR, et al. Ribosome biogenesis: a central player in cancer metastasis and therapeutic resistance. *Cancer Res*. 2022;82(13):2344-2353. doi:10.1158/0008-5472.CAN-21-4087

57. Gietz RD, Schiestl RH. High-efficiency yeast transformation using the LiAc/SS carrier DNA/PEG method. *Nat Protoc*. 2007;2(1):31-4. doi:10.1038/nprot.2007.13. PMID: 17401334.

58. Vengayil V, et al. The deubiquitinase Ubp3/Usp10 constrains glucose-mediated mitochondrial repression via phosphate budgeting. *Elife*. 2024;12:RP90293. doi:10.7554/eLife.90293

59. Walden EA, et al. Phenomic screen identifies a role for the yeast lysine acetyltransferase NuA4 in the control of Bcy1 subcellular localization, glycogen biosynthesis, and mitochondrial morphology. *PLoS Genet*. 2020;16(11):e1009220. doi:10.1371/journal.pgen.1009220

60. Yao W, et al. The INO80 complex requires the Arp5-Ies6 subcomplex for chromatin remodeling and metabolic regulation. *Mol Cell Biol*. 2016;36(6):979-91. doi:10.1128/MCB.00801-15

61. Ewels P, et al. MultiQC: summarize analysis results for multiple tools and samples in a single report. *Bioinformatics*. 2016;32(19):3047-8. doi:10.1093/bioinformatics/btw354

62. Dobin A, et al. STAR: ultrafast universal RNA-seq aligner. *Bioinformatics*. 2013;29(1):15-21. doi:10.1093/bioinformatics/bts635

63. Ge SX, et al. iDEP: an integrated web application for differential expression and pathway analysis of RNA-Seq data. *BMC Bioinformatics*. 2018;19(1):534. doi:10.1186/s12859-018-2486-6

64. Kozaeva E, et al. Model-guided dynamic control of essential metabolic nodes boosts acetyl-coenzyme A-dependent bioproduction in rewired *Pseudomonas putida*. *Metab Eng*. 2021;67:373-386. doi:10.1016/j.ymben.2021.07.014

65. Xuan Y, et al. Standardization and harmonization of distributed multi-center proteotype analysis supporting precision medicine studies. *Nat Commun*. 2020;11(1):5248. doi:10.1038/s41467-020-18904-9

66. Mori M, Let al. From coarse to fine: the absolute *Escherichia coli* proteome under diverse growth conditions. *Mol Syst Biol*. 2021;17(5):e9536. doi:10.15252/msb.20209536

67. Wiśniewski JR, et al. A "proteomic ruler" for protein copy number and concentration estimation without spike-in standards. *Mol Cell Proteomics*. 2014;13(12):3497-506. doi:10.1074/mcp.M113.037309

68. Zhang C, et al. Yeast9: a consensus genome-scale metabolic model for *S. cerevisiae* curated by the community. *Mol Syst Biol*. 2024;20(10):1134-1150. doi:10.1038/s44320-024-00060-7

69. Perez-Riverol Y, et al. The PRIDE database resources in 2022: a hub for mass spectrometry-based proteomics evidences. *Nucleic Acids Res*. 2022;50(D1):D543-D552. doi: 10.1093/nar/gkab1038

70. Sasikumar S., Sinha H. HimanshuLab/molecular-additivity-of-QTNs: v1.0. *Zenodo* 2024;https://doi.org/10.5281/zenodo.13917859

TABLES

Table 1: Unique and shared upregulated proteins in MM, TT and MMTT strains compared to the SS strain at 2h30min into sporulation.

Strains	Number of proteins	Differentially expressed proteins
MM, MMTT, TT	1	Syt1
MM, MMTT	24	Arg3, Aro10, Cox1, Cox2, Cox5a, Cul3, Fmp10, Gre1, Gtt2, Ino1, Mef1, Mrp4, Mrpl17, Mrpl7, Mrps12, Mrps35, Msf1, Pbp1, Pbp4, Rec8, Rmd9, Ssa3, Sws2, Ykl065w-A
MMTT, TT	3	Bud23, Jhd2, Ypl245w
MMTT	58	**Arg1, Arg4, Arg56**, **Arg8**, Bcs1, Cbp4, Cit3, Cmc1, Cmc2, Cox13, Cox7, Dia4, Fmp33, Gcy1, Glg1, Gpx1, Ifm1, Mam33, Mcp2, Mho1, Mhr1, Mpm1, Mrp1, Mrp7, Mrpl10, Mrpl13, Mrpl3, Mrpl35, Mrpl4, Mrpl9, Mrps16, Mrps18, Mrps28, Mrps5, Mrps8, Mrps9, Msc6, Msk1, Mss116, Pam18, Pdh1, Ppa2, Rcf1, Rim4, Rnp1, Rsm10, Rsm23, Rsm24, Rsm26, Rsm28, Rsm7, Sct1, Slm5, Trm12, Vta1, Ydr115w, Ygr021w, Yml6
MM	17	Aim32, Bop2, Cox23, Ctt1, Cyt2, Guf1, Itt1, Mdm35, Nam9, Pir3, Pot1, Pst1, Rsm19, Rsm27, Uga3, Yhr202w, Yjl045w
TT	9	Ahc1, Dal7, Hmi1, Htd2, Hym1, Lin1, Mnl1, Rme1, Yjr124c

Table 2: Difference in summed protein allocation between 2h30m and 0th hour in SS, MM, TT, and MMTT for translation, ribosome, and amino acid metabolism GO categories.

	Difference in summed mass protein allocation ($t_{2h30m} - t_{0h}$)			
Strains	**Translation (%)**	**Ribosome (%)**	**Amino acid metabolism (%)**	**Arginine metabolism (%)**
SS	-1.02	-1.14	1.68	0.11
MM	-1.42	-0.94	0.77	0.17
TT	-1.71	-1.35	1.66	0.13
MMTT	-2.52	-1.91	1.46	0.24

SUPPLEMENTARY INFORMATION

Manuscripts accompany a supplementary section that includes supplementary methods, results, figures and tables.

SUPPLEMENTARY TABLES

Table S1: List of strains used in the study

Table S2: List of primers used in the study

Table S3: Differentially expressed genes identified using Deseq2

Table S4: Differentially expressed genes identified using the Deseq2 LRT method.

Table S5: List of genes present in each cluster for SS and MMTT strain data identified using DPGP clustering

Table S6: Differentially expressed proteins MM, TT and MMTT strain at 0th hour identified in comparison to SS strain

Table S7: Differentially expressed proteins in MM, TT and MMTT strain at 2hour 30minutes identified in comparison to SS strain

Table S8: Differentially expressed proteins in SS, MM, TT and MMTT strain at 2h30minutes hour identified compared to 0th hour of each strain respectively.

Table S9: List of upregulated reactions identified using GS-DFA analysis

SUPPLEMENTARY FIGURES

Figure S1: Distinct temporal transcriptional profiles in SS and MMTT strains during sporulation (A) Heatmap representing the hierarchically clustered gene expression levels of SS and MMTT strains across 9-time points for 300 most variable genes; (B) PCA plot based on 300 most variable genes.

Figure S2: Metascape enrichment analysis reveals distinct pathway enrichment patterns between SS and MMTT strains over time. (A) Gene Ontology (GO) enrichment analysis was performed on 1,080 differentially expressed genes between SS and MMTT strains,

identified using the DESeq2 LRT method; (B-C) Heatmaps display the p-values of enriched GO terms, with hierarchical clustering applied to both rows (GO terms) and columns (clusters obtained through DPGP clustering) for SS and MMTT strains, respectively.

Figure S3: Temporal gene expression trajectories of 18 clusters of SS train obtained through DPGP clustering on gene expression profiles of DEGs obtained from the Deseq2 LRT method.

Figure S4: (A) Temporal gene expression trajectories of 17 clusters of MMTT train obtained through DPGP clustering on gene expression profiles of DEGs obtained from the Deseq2 LRT method; (B) Temporal gene expression trajectories of genes in Cluster 2 and 3 of MMTT train enriched for meiosis-specific pathways and their trajectories in SS strain.

Figure S5: PCA of the protein abundance data of SS, MM, TT and MMTT strains during the 0th hour and 2h30m into sporulation. The analysis identified one of the S288c strain replicates at 2h30m as a potential outlier, which was excluded from further analysis.

Figure S6: Differentially expressed proteins in the four strains SS, MM, TT and MMTT during the early phase of sporulation (2h30m). (A) Bar plots showing the number of significantly differentially expressed genes in comparison with the initial timepoint; (B) Venn diagrams depicting the number of proteins specifically up-regulated and down-regulated identified through comparison of the differentially expressed protein in the three phases of yeast growth; (C) Enrichment GO-terms for upregulated proteins in SS, MM, TT and MMTT strains during 2h30m in comparison with 0th hour.

Figure S7: Pairwise comparison of protein allocation between SS and allele replacement strains (MM, TT, and MMTT) for key GO-mapper terms at (A) 0h and (B) 2h30min. GO terms with significant differences in at least one pairwise comparison are shown.

Figure S8: Protein allocation to glycolysis decreases during sporulation in MMTT strain. Allocation of the whole cellular proteome to glycolysis pathway in SS, MM, TT and MMTT during the (A) 0th hour and (B) early stage of sporulation (2h30m), calculated as the mean percentage allocation. Data are means ± SD of three biological replicates (except S-2h30m, which has two replicates).

Figure S9: Mitotracker fluorescent assay on haploid S, M, T and MT and their respective *arg4*Δ and *arg56*Δ after 2h incubation in (A) YPD and (B) YPA medium.

Figure S10: The oxygen consumption rate (OCR) of SS, MM, TT and MMTT for WT (n=4), *ARG4* (n = 4) and *arg5Δ* (n = 3) cells were measured using the Seahorse Extracellular Flux 96 Analyzer grown in glucose media. After three basal measurements, sodium azide was injected into the wells to shut off mitochondrial oxygen consumption, and an additional three sets of measurements were taken.

Figure S11: Context-specific models show metabolic heterogeneity during sporulation (A) Schematic representation of steps involved in generating and analysing SNP and time-specific models; (B) The number of reactions, genes and metabolites present in each context-specific models; (C) Jaccard similarity index of context-specific models based on the presence or absence of reactions.

Figure S12. The violin plots represent the flux distribution obtained by optGpSampler for Arginosuccinate Lyase (*ARG4)* reaction during the (A) 0th hour and (B) 2h30m into sporulation in SS, MM, TT and MMTT models.

Figure S13. Steroid biosynthesis pathway is differentially activated when *MKT1*^{89G} and *TAO3*^{4477C} interact. The violin plots represent the flux distribution obtained by optGpSampler for key reactions in the steroid biosynthesis pathway during 2h30m into sporulation in SS, MM, TT and MMTT models.